43rd European Rotorcraft Forum
Milan, Italy, 12–15 September, 2017
Paper 516

TOWARDS HIGH-ORDER METHODS FOR ROTORCRAFT APPLICATIONS

Antonio Jimenez-Garcia
a.jimenez-garcia.1@research.gla.ac.uk

George N. Barakos
George.Barakos@glasgow.ac.uk

CFD Laboratory, School of Engineering
James Watt South Building
University of Glasgow, G12 8QQ, U.K.

Abstract

This work presents CFD results obtained with an efficient, high-order, finite-volume scheme. The formulation is based on the variable extrapolation MUSCL-scheme, and high-order spatial accuracy is achieved using correction terms obtained through successive differentiation. The scheme is modified to cope with physical and multiblock mesh interfaces, so stability, conservativeness, and high-order accuracy are guaranteed. Results with the proposed scheme for steady flows, showed better wake and higher resolution of vortical structures compared with the standard MUSCL, even when coarser meshes were employed. The method was also demonstrated for unsteady flows using overset and moving grids for the UH-60A rotor in forward flight and the ERICA tiltrotor in aeroplane mode. The present method adds CPU and memory overheads of 47% and 23%, respectively, in performing multi-dimensional problems for routine computations.

1 INTRODUCTION

In recent years, significant progress has been made in accurately predicting rotorcraft flows using Computational Fluid Dynamics (CFD) [1]. Nevertheless, computational aeroacoustics, and the need to resolve the wake far from rotor, call for high resolution methods, if results are to be obtained on grids of reasonable density [1, 2, 3]. In addition, since first and second-order methods are dissipative, high-order methods are needed to accurately predict vortex dominated flows problems (e.g. vortex wake of a helicopter rotor in hover [4]). However, high-order schemes may be less robust and slower to converge to steady-state solutions than low-order methods. They may also present higher memory requirements especially when implicit time stepping techniques are required.

A numerical method is K-order accurate if the solution error e is proportional to the mesh size h raised to a power K. If K is greater or equal than three, the method is considered "high-order". The reason of this criterion ($K \geq 3$) is due to the fact that most CFD solvers used in the aerospace community are second-order accurate. Given the same CPU time, high-order methods should achieve higher level of accuracy than low-order methods, and so they are more efficient.

Several types of high-order methods have been developed over the past three decades to cope with a wide range of problems. Spectral methods firstly introduced by Orszag *et al.* [5] and first-order schemes (Godunov's scheme [6]) represent the most and least accurate methods, respectively. A first classification covers high-order schemes developed either for structured [7, 8] or unstructured meshes [9, 10, 11, 12]. The formulation of those methods in finite-difference (FD) [13, 14] or finite-volume (FV) [15, 16] frameworks is also a means of classification. A more complete classification is given by Ekaterinaris [17] in his review paper.

Numerous studies in high-order methods have been formulated in the finite-difference (FD) framework [13] and is well known that FD schemes have advantages in developing high-order spatial discretisation methods.

However, they can only be applied on smooth, structured, and curvilinear meshes. In this regard, Tam *et al.* [13] developed a high-order Dispersion-Relation-Preserving (DRP) finite difference scheme, where the high-order derivatives were computed in the wave number and frequency space (using Fourier transforms) which led to preserve the dispersion relation of the scheme. Visbal *et al.* [14] applied high-order methods (up to 6th-order accurate) on a structured curvilinear mesh using implicit and compact finite-difference schemes. The method was observed to be robust through the use of a spatial filtering strategy (low-pass Pade-type non-dispersive) that smoothed the solution.

By contrast, finite-volume FV formulations are more popular for the discretisation of the fluid flow equations. Despite these methods being robust, they are typically restricted to second-order accuracy in space [18].

This paper demonstrates a high-order method (up to 4th order), which is achieved using high-order correction terms through successive differentiation [11, 12]. This scheme presents good scalability properties, which assure a low imbalance between the maximum and minimum loaded nodes when parallel performance is needed.

The structure of this paper is as follows. First, a brief description of the formulation of the high-order correction terms is presented. Then, three-dimensional steady flows around the S-76 rotor and the XV-15 tiltrotor blades are put forward, as a means of comparing the resolution of near-blade and wake flow features with low-order results with the same CFD code. Finally, the capability of the present method in preserving the wake structure for complex unsteady flows such the UH-60A rotor in forward flight and the ERICA tiltrotor in aeroplane mode is also showcased.

2 FORMULATION

This section briefly describes the formulation of the high-order correction terms. This formulation was firstly proposed by Burg [19] for unstructured finite volume codes, where a third-order spatial accuracy was achieved for two-and three-dimensional problems. Yang *et al.* [11, 12] extended the scheme to fourth-order spacial accuracy. The scheme resembles the MUSCL-schemes [20] (Monotonic Upstream-centered Scheme for Conservation Laws) and used here to discretised the convective part of the Navier–Stokes equations. It represents a one-parameter family of equations, where a third-order spatial accuracy can be achieved. The extrapolation of the flow variables to both sides of the cell-face located at $j+1/2$ for a MUSCL-scheme is given:

$$\mathbf{F}^{L}_{j+1/2} = \mathbf{F}_j + \left[\frac{\kappa_1}{2}(\mathbf{F}_{j+1} - \mathbf{F}_j) + (1-\kappa_1)\vec{\nabla}\mathbf{F}_j \bullet \vec{\mathbf{r}}_{f_j}\right] \tag{1}$$

$$\mathbf{F}^{R}_{j+1/2} = \mathbf{F}_{j+1} - \left[\frac{\kappa_1}{2}(\mathbf{F}_{j+1} - \mathbf{F}_j) + (1-\kappa_1)\vec{\nabla}\mathbf{F}_{j+1} \bullet \vec{\mathbf{r}}_{f_{j+1}}\right] \tag{2}$$

which are at least second-order accurate for all values of k_1. By setting $k_1 = 0$, a 2nd-order upwind scheme is obtained. If $k_1 = 1/3$, a third order, upwind biased scheme is derived [21]. If k_1 is set to 1, a 2nd-order central difference scheme is obtained.

In Eqns. 1 and 2, the vectors $\vec{\mathbf{r}}_{f_j}$ and $\vec{\mathbf{r}}_{f_{j+1}}$ represent the distances between the cell face $j+1/2$ and the cell-centre volumes j, and $j+1$, respectively. To reconstruct the gradient $\vec{\nabla}\mathbf{F}_j$ and $\vec{\nabla}\mathbf{F}_{j+1}$ at cell-centre volumes j and $j+1$, either Green-Gauss or Least-Squares approaches can be considered.

The proposed 4th-order structured MUSCL scheme is written as in [11], where the extrapolation to both sides of the cell-face located at $j+1/2$ is given as:

$$\mathbf{F}^{L}_{j+1/2} = \overbrace{\mathbf{F}_j + \left[\frac{\kappa_1}{2}(\mathbf{F}_{j+1} - \mathbf{F}_j) + (1-\kappa_1)\vec{\nabla}\mathbf{F}_j \bullet \vec{\mathbf{r}}_{f_j}\right]}^{\text{Standard MUSCL for the left state}} \underbrace{+\frac{1}{2}\left[\frac{\kappa_2}{2}(\vec{\nabla}\mathbf{F}_{j+1} \bullet \vec{\mathbf{r}}_{f_j} - \vec{\nabla}\mathbf{F}_j \bullet \vec{\mathbf{r}}_{f_j}) + (1-\kappa_2)\vec{\nabla}(\vec{\nabla}\mathbf{F}_j \bullet \vec{\mathbf{r}}_{f_j}) \bullet \vec{\mathbf{r}}_{f_j}\right]}_{\text{High-order corrections for the left state}} \tag{3}$$

$$\mathbf{F}^{R}_{j+1/2} = \overbrace{\mathbf{F}_{j+1} - \left[\frac{\kappa_1}{2}(\mathbf{F}_{j+1} - \mathbf{F}_j) + (1-\kappa_1)\vec{\nabla}\mathbf{F}_{j+1} \bullet \vec{\mathbf{r}}_{f_{j+1}}\right]}^{\text{Standard MUSCL for the right state}} \underbrace{+\frac{1}{2}\left[\frac{\kappa_2}{2}(\vec{\nabla}\mathbf{F}_{j+1} \bullet \vec{\mathbf{r}}_{f_{j+1}} - \vec{\nabla}\mathbf{F}_j \bullet \vec{\mathbf{r}}_{f_{j+1}}) + (1-\kappa_2)\vec{\nabla}(\vec{\nabla}\mathbf{F}_{j+1} \bullet \vec{\mathbf{r}}_{f_{j+1}}) \bullet \vec{\mathbf{r}}_{f_{j+1}}\right]}_{\text{High-order corrections for the right state}} \tag{4}$$

As can be observed, this new variable extrapolation formulation represents a two-parameter family (k_1 and k_2). As shown in Eqns. 3 and 4, the high-order correction terms have been developed using a Taylor series expansion about the centre of the face $j+1/2$, which requires knowledge of its second derivates $\vec{\nabla}\left(\vec{\nabla}\mathbf{F}_j \bullet \vec{\mathbf{r}}_{f_j}\right)$ and $\vec{\nabla}\left(\vec{\nabla}\mathbf{F}_{j+1} \bullet \vec{\mathbf{r}}_{f_{j+1}}\right)$. Once the first derivatives are computed, the second derivatives can be estimated by successive application of the Green-Gauss or Least Squares Method to the first derivatives. The three normal and cross second derivatives $\left(\frac{\partial^2 F}{\partial x^2}, \frac{\partial^2 F}{\partial y^2}, \frac{\partial^2 F}{\partial z^2}, \frac{\partial^2 F}{\partial xy}, \frac{\partial^2 F}{\partial xz}, \frac{\partial^2 F}{\partial yz}\right)$ need to be allocated in the same way like the first derivatives, adding a memory overhead when high-order is used, in the current data structure of the HMB solver [22, 23, 24] that is used in this work. This also implies that further communication between processors is needed for parallel execution.

Further information about the optimal values of k_1 and k_2 to assure higher-order of accuracy, spectral properties of the proposed 4th-order scheme using Fourier analysis, and details of the implementation can be found in a recent publication [25].

3 RESULTS

In this section, numerical simulations with the high-order scheme are presented. Table 1 lists the test cases used in the validation of the present high-order scheme.

Steady and unsteady solutions were computed on 96 and 240 cores, respectively, of the high performance computer clusters Jupiter of Glasgow University and

ARCHIE-WeSt. The present high-order method adds CPU and memory overheads of 47% and 23%, respectively, in performing 3D problems using the same number of time steps.

3.1 S-76 helicopter blade in hover

In this section, the flow around the 1/4.71 scale S-76 rotor blade, in hover, is computed using the MUSCL-2 and MUSCL-4 schemes. Due to the public availability of the case, and data sets with various tip shapes, the AIAA Applied Aerodynamics Rotor Simulations Working Group [26, 27, 28, 29] was established in 2014 to evaluate the current state-of-the-art performance prediction using different CFD solvers and methods for the same blade geometry. Therefore, this blade has been extensively studied [30, 31, 32, 33, 34] and represents a benchmark for the validation of schemes.

The four-bladed S-76 model rotor, of 1/4.71 scale, has -10° of lineal twist, and three aerofoil sections comprise its planform: the SC-1013-R8 is used from the root of the blade up to 18.9% R, the SC-1095-R8 aerofoil is used from 40% R to 80% R, and the SC-1095 aerofoil is used from 84% R to the tip. For this study, the planform of the S-76 model rotor with 60% taper and 35° swept tip is selected at a scale of 1/4.71. The main characteristics of the model rotor blades are summarised in Table 2.

A mesh generated using the chimera technique was used for the design study of the S-76 rotor, composed of a periodic background mesh and a component mesh for the blade (see Figure 1 (a)). As the S-76 is a four-bladed rotor, only a quarter of the domain was meshed. A C-topology around the leading edge of the blade was selected, whereas an H-topology was employed at the trailing edge of the blade (see Figure 1 (b)). Coarse and medium grids were built. Table 3 shows a breakdown of the number of cells (per blade) used for the background mesh, and for the body-fitted mesh around the S-76 rotor blade.

The blade-tip Mach number was set to 0.65 and three blade pitch angles were considered, corresponding to low, medium, and high thrust. The Reynolds number, based on the reference blade chord of 3.1 inches and on the tip speed, was $1.18 \cdot 10^6$. All flow solutions were computed by solving the RANS equations, with Menter's k-ω SST turbulence model [35]. The flow equations were integrated with the implicit dual-time stepping method of HMB.

The effect of the spatial discretisation on the Figure of Merit (FoM) and torque coefficient (C_Q) as a function of the blade loading coefficient C_T/σ is shown in Figures 2 (a) and (b), respectively. Vertical lines are labelled as empty (3,177 kg) and maximum gross (5,307 kg) weight, define the hovering range of the S-76 helicopter rotor. CFD solutions were obtained with the MUSCL-2 and MUSCL-4 schemes using a coarse (red and black lines, respectively) and medium grids (green solid lines and purple deltas, respectively). The test data of Balch and Lombardi [36] are represented by opened squares. The ability to resolve the vortex structure at the background level is key for accurate predictions of the loading on the blade. Hence, half million cells were added to the new background mesh (see Table 3). Consequently, the medium mesh shows a better agreement at low, medium, and high thrust coefficients with the test data of Balch and Lombardi [36]. Results obtained with the MUSCL-4 scheme and the coarse mesh show a very good agreement with the experimental data and with the MUSCL-2 scheme with the medium grid.

3.2 XV-15 tiltrotor blade

This section demonstrates the performance of the MUSCL-4 scheme with the chimera technique for a three-dimensional tiltrotor flow. This highly loaded rotor can produce strong wakes. The resolution of which may benefit from a higher-order scheme.

The flow around the three-bladed XV-15 rotor [37] is solved in hover by casting the equations as a steady-state problem in a noninertial reference frame. The MUSCL-4 scheme is compared with the scheme MUSCL-2 in terms of integrated airloads (FoM, C_T, and C_Q) and visualisation of the wake flow features. All flow solutions were computed using the RANS equations and Menter's k-ω SST turbulence model [35]. The flow equations were integrated with the implicit dual-time stepping method of HMB.

The three-bladed XV-15 rotor geometry comprises NACA 6-series five-digit aerofoil sections, and its main geometric characteristics [37] are summarised in Table 4. Regarding the test conditions, the blade-tip Mach number was set to 0.69, and five blade pitch angles were considered ($\theta_{75} = 3^\circ, 5^\circ, 7^\circ, 10^\circ$, and 13°), corresponding to low, medium, and high disc loadings. The Reynolds number, based on the reference blade chord of 14 inches and on the tip speed, was $4.95 \cdot 10^6$.

The computational domain was composed by a cylindrical off-body mesh used as a background (Figure 3 (a)), and a body-fitted mesh for the blade with a C-H topology (Figure 3 (b)). Table 5 lists the grids used and the breakdown of cells per blade. Coarse and medium meshes have 6.2 and 9.6 million cells per blade (equivalent to 18.6 and 28.8 million cells for three blades), with the same grid resolution for the body-fitted mesh (3.6 million cells). The background mesh, however, was refined at the wake and near-body regions, increasing the grid size from 2.6 to 6 million cells. Solutions were obtained with the MUSCL-2 scheme using the coarse and medium grids, whilst the MUSCL-4 was only employed with the coarse grid.

Figure 4 shows the effect of the MUSCL-2 and MUSCL-4 schemes on the FoM and C_Q for the full-scale XV-15 rotor. Experimental data is also shown, carried out by Felker *et al.* [38] at the Outdoor Aeronautic Research Facility (OARF), and Light [39] and Betzina [37] at the NASA 80×120ft wind tunnel. Vertical lines labelled as empty (4,574 kg) and maximum gross (6,000

kg) weight, define the hovering range of the XV-15 helicopter rotor [40]. Momentum-based estimates of the FoM [41] are also included, where an induced power factor k_i of 1.1 and overall profile drag coefficient C_{D0} of 0.01 were used. Polynomial fit curves were computed using the obtained CFD results and shown with solid lines and squares (MUSCL-2 with a coarse grid), deltas (MUSCL-2 with a medium grid), and triangles (MUSCL-4 with a coarse grid). The CFD results obtained with the MUSCL-2 scheme present a good agreement with the test data of Betzina [37] for all blade pitch angles. Moreover, the effect of the grid size has a mild effect on the overall performance at low thrust, with a small influence at high thrust. Regarding the results obtained with the MUSCL-4 scheme, a good agreement was obtained if compared with the MUSCL-2 scheme when using a medium grid, and the experimental data of Betzina.

To assess the ability of the MUSCL-4 scheme in accurately predicting the loads when a coarse mesh is employed, a comparison between predicted and measured [42, 43] FoM at a blade pitch angle of 10° is reported in Table 6. Predictions with the MUSCL-2 scheme using coarse and medium grids indicate good correlation with the experiments (1.5 and 0.8 counts of FoM, respectively). Results obtained with the MUSCL-4 scheme on a coarse grid present a small discrepancy of 0.5 counts of FoM, which highlights the benefit of using higher-order numerical scheme in accurately predicting integrated airloads.

Despite that the lower-order numerical scheme is sufficient to predict the loads over the blades [44], it did not preserve the near-blade and wake flow features. In hover, to ensure realistic predictions of the wake-induced effects and therefore induced-drag, the radial and vertical displacements of the vortex core should be resolved, at least for the first and second wake passages.

Figure 5 shows the wake of the full-scale XV-15 rotor using iso-surfaces of $\bar{Q}$-criterion obtained with MUSCL-2 (a) and MUSCL-4 (b) with the same coarse grid of Table 5. It should be mentioned that, a blade pitch angle of 10° degrees was selected for such comparison. It is observed that the MUSCL-4 scheme preserves much better the helical vortex filaments that trail from each blade tip, and the shear layers trailed from the trailing edge of the blade, compared with the MUSCL-2 solution. Therefore, the lower dissipation of the MUSCL-4 scheme results in an improved preservation of rotor wake structures. In this regard, if the MUSCL-2 is employed, the vorticity of the vortex cores (computed using the local vorticity maximum criterion) is more dissipated at a wake age of $2\pi/3$ (first blade passage in Figure 6) if compared with MUSCL-4 results. Likewise, at wake ages of $4\pi/3$ (second blade passage) and 2π (third blade passage) a reduction of vorticity by 42.8% and 45.2% is observed when MUSCL-2 is employed.

3.3 UH-60A rotor in forward flight

To validate the present high-order scheme for a three-dimensional unsteady flow with overset and moving grids, the UH-60A rotor in forward flight was also considered. The UH-60A is a four-bladed rotor made of two aerofoil profiles; the SC-1095 and SC-1095R [45]. The planform of the UH-60A rotor features a 20° swept tip which covers 6% of the blade's radius, with a -16° of linear twist. The main geometric characteristics of the UH-60A blade [36, 46, 47] are summarised in Table 7.

The multi-block structured grid for the full rotor has a total of 42.2 million cells with 2,064 blocks, with 42.2 and 8.2 million cells for the background and body-fitted grids, respectively. A hub was also included in the computational domain and modelled as a generic ellipsoidal surface.

The test case selected for validation corresponds to the UH-60A main rotor at high-speed forward flight. Flight test data corresponding to this demanding configuration (flight C8534) was acquired by the U.S. Army/NASA UH-60A Airloads Program [48]. The rotor advance ratio was μ= 0.368, and the freestream Mach number was set to 0.236. To meet the target thrust coefficient C_T/σ= 0.08 while having zero roll and pitch moments, a matrix trimming method is used in HMB [49], which uses the blade-element momentum theory to compute the elements of the sensitivity matrix. The flow solutions corresponding to MUSCL-2 and MUSCL-4 schemes were computed by solving the URANS equations, coupled with Menter's k-ω SST turbulence model [35]. The time step corresponds to 0.25 deg in the azimuthal direction and was based on the experience gained with previous rotor computations in forward flight [50]. Comparisons of the blade normal force and pitch moment (mean removed) at three radial stations is shown in Figure 7. Good agreement is found between experimental and predicted load with similar trend between MUSCL-2 and MUSCL-4 results.

Visualisation of the flowfield of the UH-60A rotor using the $\bar{Q}$-criterion [51] is presented in Figure 8 for the MUSCL-2 and MUSCL-4 solutions. The wake obtained with MUSCL-4 solution is preserved for much longer than the one obtained with MUSCL-2. Figure 9 shows vorticity contours at the planes x/R= 0.5, 1, and 2 for the MUSCL-2 and MUSCL-4 schemes. Results with MUSCL-4 show a higher resolution of the rotor wake structures at the advancing and retreating sides if compared with the MUSCL-2. In fact, the vortex C ($\psi = 270^\circ$) computed with MUSCL-2 in Figure 9 (a) and (c) shows a reduction of the core vorticity by almost 20% with respect to the MUSCL-4 results. Regarding the plane x/R= 2 (see Figure 9 (e)-(f)), it highlights the ability of the MUSCL-4 scheme in preserving the vortex cores and rotor wake structures A and B, even far away from the rotor.

3.4 ERICA tiltrotor in aeroplane mode

To demonstrate that the current scheme can deliver on complex cases, a complete tiltrotor is simulated. Numerical simulations of the ERICA tiltrotor using the MUSCL-2 and MUSCL-4 schemes were performed and are presented here. The ERICA tiltrotor is a tiltwing aircraft, where a small part of the wing can be partially rotated to mitigate the strong aerodynamic interaction between rotor and wing and to reduce the downward force acting on the wings in hover. In this regard, the research project NICETRIP [52] (Novel Innovative Competitive Effective Tilt Rotor Integrated Project) was funded by the European Union (EU) to develop a database covering aerodynamic interactional phenomena and other technological aspects of tiltwing vehicles. In this framework, a 1:5 motorised model-scale tiltrotor was designed and manufactured under the name of ERICA (Enhanced Rotorcraft Innovative Concept Achievement) [53] and experiments were undertaken using the 9.5$\times$9.5m DNW-LLF (German-Dutch Wind Tunnels Large Low-speed Facility) and the 8m S1MA ONERA wind tunnels. For this study, an aeroplane configuration was selected, where the rotor blades were fully resolved.

The chimera method was employed to ease the generation of the different structured multi-block grids. Self-contained component grids for the main fuselage and the nacelle-tiltable wing were built, while four ADYN blades were embedded in the nacelle mesh component. A Cartesian off-body mesh was used as background to capture the convection of the tip vortex generated by the blades. Table 8 compares the mesh size used here for CFD computation. The multi-block overset arrangement of the ERICA tiltrotor for the aeroplane mode is shown in Figure 10.

Table 9 summarises the test conditions employed for computations. The aeroplane mode is labelled as AC1 (aeroplane configuration), and refers to a very low speed aeroplane-mode M_∞= 0.168, along with a large aircraft AoA of δ_{FU}= 10.02 degrees. Neither the nacelles nor the tiltable wings were tilted with respect to the fuselage (δ_{FU}= δ_{NAC}= δ_{TW}). The Reynolds numbers, based on the reference length L_{ref} and on the freestream velocity V_∞, was $1.70 \cdot 10^6$.

Four cross-sections were selected for C_P profile comparisons between CFD and experiments [54, 55] (see Table 10). One section was selected on the top symmetry planes of the fuselage (labelled with SYM-TOP), one section on the fixed wing (labelled with FW), and two on the tiltable wing (labelled with TW) which define the zone of aerodynamic interaction between the tiltable wing and the blades.

C_P profile comparisons between CFD and experiments [54, 55] on the fuselage, fixed and tiltable wings of the ERICA tiltrotor are given in Figure 11. They correspond to the top fuselage centre-line and inner, middle, and outer tiltable and fixed wing sections. The CFD results were not averaged in phase, which could lead to a source of error in the comparison since all test data is phase averaged. For both cases, C_P values were averaged over the last computed rotor revolution instead of time-averaging. Regarding the C_P profile at the centre-line of the fuselage (Figure 11 (a)), a zone of recirculation is seen by both sets of experiments (Modane and DNW experiments are denoted by squares and triangles, respectively) represented by a pressure plateau after the wing leading edge suction peak. The HMB predictions (MUSCL-2=red line, MUSCL-4=green line) overestimate the suction peak and do not capture the region of recirculation. This can be due to a failure of the employed turbulence model, wind tunnel effects, and lack of exact, trimmed, conditions for the simulation.

In the middle fixed and tiltable wing sections (Figures 11 (c) and 11 (d)), wind tunnel experiments show a good agreement, with small differences of 9% for the suction peak. Note that the differences between the two sets of experiments are always larger than the differences between the MUSCL-2 and MUSCL-4 results.

Regarding the MUSCL-2 solution, the wake behind the rotor disk (see Figure 12 (a)) is preserved for more than one rotor diameter downstream. This informative plot shows the interaction of the rotor wake with the nacelle and tiltable wings. From these iso-surfaces it can be seen that the rotor wake does not directly interact with the fuselage and the fixed part of the wings. Iso-surface contours of $\bar{Q}$-criterion are shown from the CFD simulations using the MUSCL-4 scheme in Figure 12 (b), which reveals that a detailed wake characteristics can be easily identified when using high-order schemes.

4 CONCLUSIONS

The implementation of a high-order, finite-volume scheme in the HMB CFD Solver has been presented. The scheme has showed a higher level of accuracy if compared with the standard-MUSCL, and 4th-order accuracy was achieved on Cartesian grids. Furthermore, a significantly high spectral resolution (dispersion and dissipation) of the new scheme is observed. Three-dimensional test cases have been considered to demonstrate the new formulation. Results of the steady flow around the S-76 and XV-15 blades showed a better wake and higher resolution of the vortical structures compared with the standard MUSCL solution. The method was also demonstrated for three-dimensional unsteady flows using overset and moving grid computations for the UH-60A rotor in forward flight and the ERICA tiltrotor in aeroplane mode. The present method adds CPU and memory overheads of 47% and 23%, respectively, in performing multi-dimensional problems, which encourages the use of this high-order method for routine computations.

5 ACKNOWLEDGMENTS

Some results were obtained using the EPSRC funded ARCHIE-WeSt High Performance Computer (www.archie-west.ac.uk), EPSRC grant no. EP/K000586/1. Part of this work is funded under the HiperTilt Project of the UK Technology Strategy Board (TSB) and Leonardo Helicopters under Contract Nr. 101370.

6 REFERENCES

[1] Liu, Y., Anusonti-Inthra, P., and Diskin, B., "Development and Validation of a Multidisciplinary Tool for Accurate and Efficient Rotorcraft Noise Prediction," NASA CR–2011-217057, Feb. 2011.

[2] Wang, Z. J., Fidkowski, K., Abgrall, R., Bassi, F., Caraeni, D., Cary, A., Deconinck, H., Hartmannn, R., Hillewaert, K., Huynh, H. T., Kroll, N., May, G., Persson, P.-O., van Leer, B., and Visbal, M., "High-Order CFD Methods: Current Status and Perspective," *International Journal for Numerical Methods in Fluids*, Vol. 72, No. 8, 2013, pp. 811–845, DOI: 0.1002/fld.3767.

[3] Kroll, N., Bieler, H., Deconinck, H., Couaillier, V., van der Ven, H., and Sorensen, K., "ADIGMA - a European initiative on the development of adaptive higher-order variational methods for aerospace applications," *Notes on Numerical Fluid Mechanics and Multidisciplinary Design*, Vol. 113, 2010.

[4] Jimenez-Garcia, A. and Barakos, G. N., "CFD Analysis of Hover Performance of Rotors at Full and Model-Scale Conditions," *Aeronautical Journal*, Vol. 120, No. 1231, 2016, pp. 1386–1424, DOI:10.1017/aer.2016.58.

[5] Gottlieb, S. and Orszag, A., *Numerical Analysis of Spectral Methods: Theory and Applications*, SIAM: Philadelphia, 1977.

[6] Godunov, S. K., "A finite-difference method for the numerical computation of discontinuous solutions of the equations of fluid dynamics," *Matematicheski Sbornik*, Vol. 47, No. 3, 1959, pp. 271–306.

[7] Lele, S. K., "Compact Finite Difference Schemes with Spectral-like Resolution," *Journal of Computational Physics*, Vol. 103, No. 1, 1992, pp. 16–42, DOI: 10.1016/0021-9991(92)90324-R.

[8] Liu, X., Osher, S., and Chan, T., "Weighted essentially non-oscillatory schemes," *Journal of Computational Physics*, Vol. 115, No. 1, 1994, pp. 200–212, DOI: 10.1006/jcph.1994.1187.

[9] Barth, T. and Frederickson, P., "High-order Solution of the Euler Equations on Unstructured Grids Using Quadratic Reconstruction," *AIAA Journal*, Vol. 90, No. 13, 1990, DOI: 10.2514/6.1990-13.

[10] Nogueira, X., Colominas, I., Cueto-Felgueroso, L., Khelladi, S., Navarrina, F., and Casteleiro, M., "Resolution of computational aeroacoustics problems on unstructured grids with a higher-order finite volume scheme," *Journal of Computational and Applied Mathematics*, Vol. 234, No. 7, 2010, pp. 2089–2097, DOI: 10.1016/j.cam.2009.08.067.

[11] Yang, H. Q., Chen, Z. J., Przekwas, A., and Dudley, J., "A high-order CFD method using successive differentiation," *Journal of Computational Physics*, Vol. 281, No. 1, 2015, pp. 690–707, DOI: 10.1016/j.jcp.2014.10.046.

[12] Yang, H. Q. and Harris, R. E., "Vertex-centered, high-order schemes for turbulent flows," *Proceedings of the Fifty-Fourth Aerospace Sciences Meeting*, AIAA, San Diego, California, 2016, pp. 1–24.

[13] Tam, C. K. W. and Webb, J. C., "Dispersion-relation-preserving finite difference schemes for computational acoustics," *Journal of Computational Physics*, Vol. 107, No. 2, 1993, pp. 262–281, DOI: 10.1006/jcph.1993.1142.

[14] Visbal, M. R. and Gaitonde, D. V., "High-order accurate methods for complex unsteady subsonic flows," *AIAA Journal*, Vol. 37, No. 10, 1999, pp. 1231–1239, DOI: 10.2514/2.591.

[15] McCorquodale, P. and Colella, P., "A High-Order Finite-Volume Method for Conservation Laws on Locally Refined Grids," *Communications in Applied Mathematics and Computational Science*, Vol. 6, No. 1, 2011, pp. 1–25, DOI: 10.2140/camcos.2011.6.1.

[16] Colella, P., Dorr, M. R., Hittinger, J. A. F., and Martin, D. F., "High-Order, finite-volume methods in mapped coordinates," *Journal of Computational Physics*, Vol. 230, No. 8, 2011, pp. 2952–2976, DOI: 10.1016/j.jcp.2010.12.044.

[17] Ekaterinaris, J. A., "High-order accurate, low numerical diffusion methods for aerodynamics," *Progress in Aerospace Sciences*, Vol. 41, No. 1, 2005, pp. 192–300, DOI: 10.1016/j.paerosci.2005.03.003.

[18] Calhoun, D. A., Helzel, C., and Leveque, R. J., "Logically rectangular grids and finite volume methods for PDEs in circular and spherical domains," *SIAM Rev.*, Vol. 50, No. 4, 2008, pp. 723–752, DOI: 10.1137/060664094.

[19] Burg, C. O. E., "Higher Order Variable Extrapolation For Unstructured Finite Volume RANS Flow Solvers," *Proceedings of the Seventieth AIAA Computational Fluid Dynamics Conference*, AIAA, Toronto, Ontario, 2005, pp. 1–17.

[20] van Leer, B., "Towards the Ultimate Conservative Difference Scheme. V. A Second-Order Sequel to Godunov's Method," *Journal of Computational Physics*, Vol. 32, No. 1, 1979, pp. 101–136, DOI: 10.1016/0021-9991(79)90145-1.

[21] Anderson, W. K., Thomas, J. L., and van Leer, B., "Comparison of Finite Volume Flux Vector Splittings for the Euler Equations," *AIAA Journal*, Vol. 24, No. 9, 1986, pp. 1453–1460, DOI: 10.2514/3.9465.

[22] Jimenez-Garcia, A. and Barakos, G. N., "Accurate predictions of rotor hover performance at low and high disc loadings," *Journal of Aircraft*, 2017, DOI: 10.2514/1.C034144, Early online publication.

[23] Jimenez-Garcia, A. and Barakos, G. N., "Numerical simulations on the ERICA tiltrotor," *Aerospace Science and Technology*, Vol. 64, No. 1, 2017, pp. 171–191, DOI: 10.1016/j.ast.2017.01.023.

[24] Barakos, G. N. and Johnson, C. S., "Acoustic Comparison of Propellers," *International Journal of Aeroacoustics*, Vol. 15, No. 6, 2016, pp. 575–594, DOI: 10.1177/1475472X16659214.

[25] Jimenez-Garcia, A. and Barakos, G. N., "Implementation of High-Order Methods in the HMB CFD Solver," *Proceedings of the 73rd American Helicopter Society Annual Forum*, AHS, Fort Worth, Texas, 2017, pp. 1–19.

[26] Hariharan, N., Egolf, A., and Sankar, L., "Simulation of Rotor in Hover: Current State and Challenges," *Proceedings of the 52nd Aerospace Sciences Meeting*, AIAA-2014-0041, National Harbor, Maryland, 2014, pp. 1–28.

[27] Hariharan, N., Egolf, A., and Sankar, R. N. L., "Helicopter Rotor Aerodynamic Modeling in Hover:AIAA Standardized Hover Evaluations," *Proceedings of the 53rd Aerospace Sciences Meeting*, AIAA-2015-1242, Kissimmee, Florida, 2015, pp. 1–34.

[28] Hariharan, N., Narducci, R., Reed, E., and Egolf, T. A., "Helicopter Aerodynamic Modeling of Rotor with Tip-Shape Variations: AIAA Standardized Hover Evaluations," *Proceedings of the 54th Aerospace Sciences Meeting*, AIAA-2016-0031, San Diego, California, 2016, pp. 1–42.

[29] Egolf, T. A., Hariharan, N., Narducci, R., and Reed, E., "AIAA Standardized Hover Simulation: Hover Performance Prediction Status and OUtstanding Issues," *Proceedings of the 55th Aerospace Sciences Meeting*, AIAA-2017-1429, Grapevine, Texas, 2017, pp. 1–14.

[30] Baeder, J. D., Medida, S., and Kalra, T. S., "OVERTURNS Simulations of S-76 Rotor in Hover," *Proceedings of the 52nd Aerospace Sciences Meeting*, AIAA-2014-0045, National Harbor, Maryland, 2014, pp. 1–11.

[31] Jain, R. K. and Potsdam, M. A., "Hover Predictions on the Sikorsky S-76 Rotor using Helios," *Proceedings of the 52nd Aerospace Sciences Meeting*, AIAA-2014-0207, National Harbor, Maryland, 2014, pp. 1–21.

[32] Sheng, C., Zhao, Q., and Wang, J., "S-76 Rotor Hover Prediction Using U2NCLE Solver," *Proceedings of the 52nd Aerospace Sciences Meeting*, AIAA-2014-0044, National Harbor, Maryland, 2014, pp. 1–19.

[33] Narducci, R., "OVERFLOW Simulation of Rotors in Hover: The Boeing Company," *Proceedings of the Fifty-Second Aerospace Sciences Meeting*, AIAA-2014-0208, National Harbor, Maryland, 2014, pp. 1–9.

[34] Jimenez, A. and Barakos, G. N., "Hover Performance Predictions for the S-76 Main Rotor Blade," *Proceedings of the 53rd Aerospace Sciences Meeting*, AIAA-2015-1712, Kissimmee, Florida, 2015, pp. 1–34.

[35] Menter, F. R., "Two-Equation Eddy-Viscosity Turbulence Models for Engineering Applications," *AIAA Journal*, Vol. 32, No. 8, 1994, pp. 1598–1605, DOI: 10.2514/3.12149.

[36] Balch, D. T. and Lombardi, J., "Experimental Study of Main Rotor Tip Geometry and Tail Rotor Interactions in Hover. Vol I - Text and Figures," NASA CR–177336, Feb. 1985.

[37] Betzina, M. D., "Rotor Performance of an Isolated Full-Scale XV-15 Tiltrotor in Helicopter Mode," *Proceedings of the American Helicopter Society Aerodynamics, Acoustics, and Test and Evaluation Technical Specialist Meeting*, AHS, San Francisco, CA, 2002, pp. 1–12.

[38] Felker, F. F., Betzina, M. D., and Signor, D. B., "Performance and Loads Data from a Hover Test of a Full-Scale XV-15 Rotor," NASA TM–86833, Sept. 1985.

[39] Light, J. S., "Results from an XV-15 Rotor Test in the National Full-Scale Aerodynamics Complex," *Proceedings of the 53rd American Helicopter Society Annual Forum*, AHS, Virginia Beach, Virginia, 1997.

[40] Maisel, M. D., Giulianetti, D. J., and Dugan, D. C., "The History of the XV-15 Tilt Rotor Research Aircraft: From Concept to Flight," NASA SP-2000-4517, 2000.

[41] Leishman, J. G., *Principles of Helicopter Aerodynamics*, Cambridge, 2000.

[42] Wadcock, A. J., Yamauchi, G. K., and Driver, D. M., "Skin Friction Measurements on a Hovering Full-Scale Tilt Rotor," *Journal American Helicopter Society*, Vol. 99, No. 4, 1999, pp. 312–319.

[43] Yoon, S., Pulliam, T. H., and Chaderjian, N. M., "Simulations of XV-15 Rotor Flows in Hover Using OVERFLOW," *Proceedings of the 50th AHS Aeromechanics Specialists*, AHS, San Francisco, CA, 2014, pp. 1–11.

[44] Ghosh, D., *Compact-Reconstruction Weighted Essentially Non-Oscillatory Schemes for Hyperbolic Conservation Laws*, Ph.D. thesis, University of Maryland, United States, Jan. 2013.

[45] Bousman, W. G., "Aerodynamic Characteristics of SC1095 and SC1094R8 Airfoils," NASA TP–2003-212265, Dec. 2003.

[46] Shinoda, P. M., Yeo, H., and Norman, T. R., "Rotor Performance of a UH-60 Rotor System in the NASA Ames 80- by 120-Foot Wind Tunnel," *Proceedings of 58th American Helicopter Society*, AHS, Montreal, Canada, 2002, pp. 1–18.

[47] Dindar, M., Shephard, M. S., Flaherty, J. E., and Jansen, K., "Adaptive CFD analysis for rotorcraft aerodynamics," *Computer Methods in Applied Mechanics and Engineering*, Vol. 189, No. 1, 2000, pp. 1055–1076, DOI: 10.1016/S0045-7825(99)00368-0.

[48] Kufeld, R., Balough, D., Cross, J., Studebaker, K., and Jennison, C., "Flight Testing the UH-60A Airloads Aircraft," *Proceedings of 50th American Helicopter Society*, AHS-50-1994-044, Alexandria, Virginia, 1994, pp. 1–22.

[49] Steijl, R., Barakos, G. N., and Badcock, K., "A Framework for CFD Analysis of Helicopter Rotors in Hover and Forward Flight," *International Journal for Numerical Methods in Fluids*, Vol. 51, No. 8, 2006, pp. 819–847, DOI: 10.1002/fld.1086.

[50] Steijl, R., Barakos, G. N., and Badcock, K. J., "Computational Study of the Advancing-Side Lift-Phase Problem," *Journal of Aircraft*, Vol. 45, No. 1, 2008, pp. 246–257, DOI: 10.2514/1.22044.

[51] Jeong, J. and Hussain, F., "On the identification of a vortex," *Journal of Fluid Mechanics*, Vol. 285, 1995, pp. 69–94, DOI: 10.1017/S0022112095000462.

[52] "NICETRIP - Novel Innovative Competitive Effective Tilt Rotor Integrated Project: NICETRIP website," http://www.transport-research.info/project/novel-innovative-competitive-effective-tilt-rotor-integrated-project, last visited date: 29/09/2016.

[53] Alli, P., Nannoni, F., and Cicalé, M., "ERICA: The European Tiltrotor Design and Critical Technology Projects," *AIAA/ICAS, International Air and Space Symposium and Exposition: The Next 100 Years*, Day-ton, Ohio, USA, 2005.

[54] Philipsen, I. and Heinrich, S., "Test Report on Measurements on the NICETRIP Large-Scale Powered Model in DNW-LLF," Project number 2410.1338, Aug. 2013.

[55] Lebrun, F., "NICETRIP test - ERICA 1/5th scale powered model in the test section no.2 - $45m^2$ of S1MA wind tunnel," Test Report Number PV 1/17648 DSMA, June 2014.

[56] Bruin, A. and Schneider, O., "A Discussion of Measured Static and Dynamic Rotor Loads During Testing of the ERICA Tilt-Wing Rotorcraft Configuration in DNW-LLF Wind Tunnel," *Proceeding of the 40th European Rotorcraft Forum*, ERF, Southampton, UK, 2014, pp. 1–15.

[57] Vigevano, L., Beaumier, P., Decours, J., Khier, W., Kneisch, T., and Vitagliano, P., "Tilt-Rotor Aerodynamics Activities During the NICETRIP Project," *Proceeding of the 40th European Rotorcraft Forum*, ERF, Southampton, UK, 2014, pp. 1–14.

7 TABLES AND FIGURES

Table 1: List of test cases used in the validation of high-order methods.

Test Case	Equations	Steady/Unsteady
S-76 rotor	Navier-Stokes (3D)	Steady
XV-15 tiltrotor	Navier-Stokes (3D)	Steady
UH-60A	Navier-Stokes (3D)	Unsteady
ERICA tiltrotor	Navier-Stokes (3D)	Unsteady

Table 2: Geometric properties of the 1/4.71 scale S-76 rotor [36].

Parameter	Value
Number of blades, N_b	4
Rotor radius, R	56.04 inches
Reference blade chord, c_{ref}	3.1 inches
Aspect ratio, R/c_{ref}	18.07
Rotor solidity, σ	0.0704
Linear twist angle, Θ	-10°

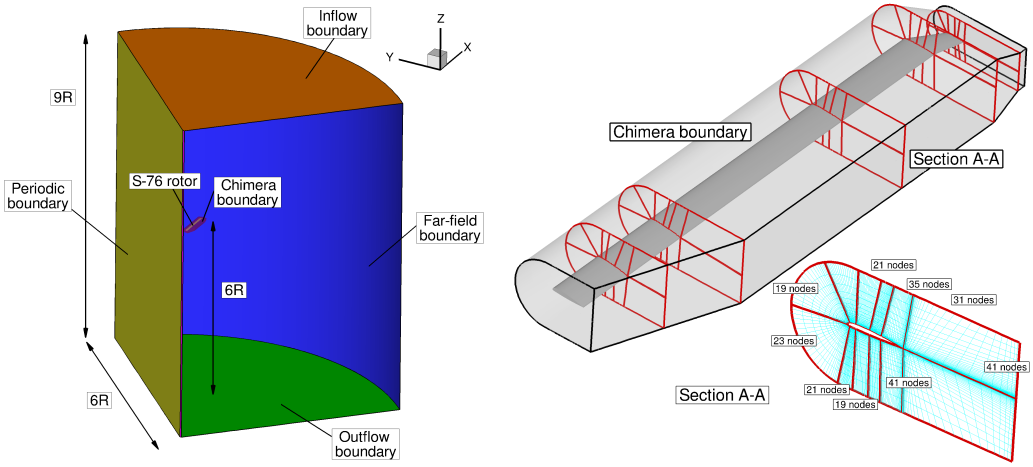

(a) Computational domain. (b) S-76 rotor mesh.

Figure 1: Computational domain and boundary conditions employed (left) and detailed view of the body-fitted S-76 rotor mesh (right).

Table 3: Mesh size in million cells for the S-76 rotor mesh.

	Coarse Mesh	Medium Mesh
Background mesh size	2 million	3.5 million
Blade mesh size	3 million	4 million
Overall mesh size	5 million	7.5 million
Wall distance	$1.0 \cdot 10^{-5} c_{\text{ref}}$	$1.0 \cdot 10^{-5} c_{\text{ref}}$

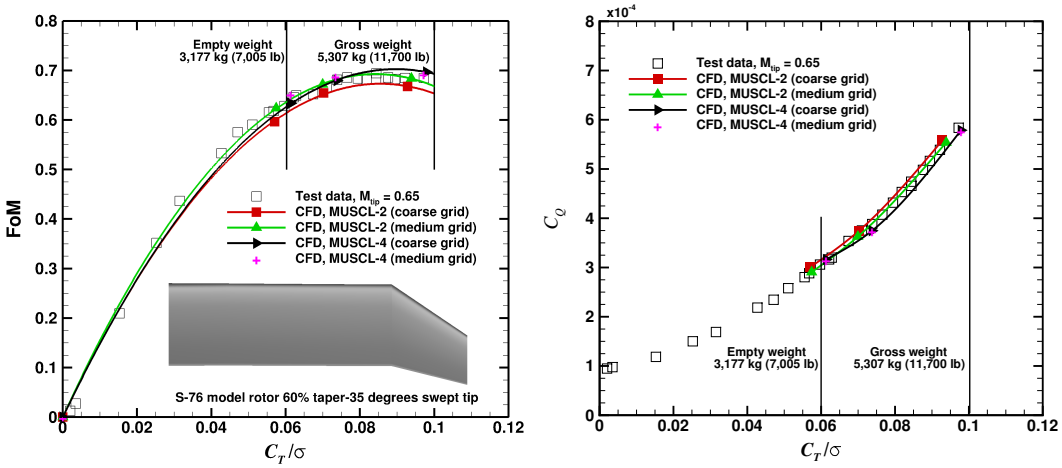

(a) C_T/σ - FoM. (b) C_T/σ - C_Q.

Figure 2: Effect of the MUSCL-2 and MUSCL-4 schemes on the figure of merit (left) and torque coefficient (right) for the 1/4.71 scale S-76 rotor blade.

Table 4: Geometric properties of the full-scale XV-15 rotor [37].

Parameter	Value
Number of blades, N_b	3
Rotor radius, R	150 inches
Reference blade chord, c_{ref}	14 inches
Aspect ratio, R/c_{ref}	10.71
Rotor solidity, σ	0.089
Linear twist angle, Θ	-40.25°

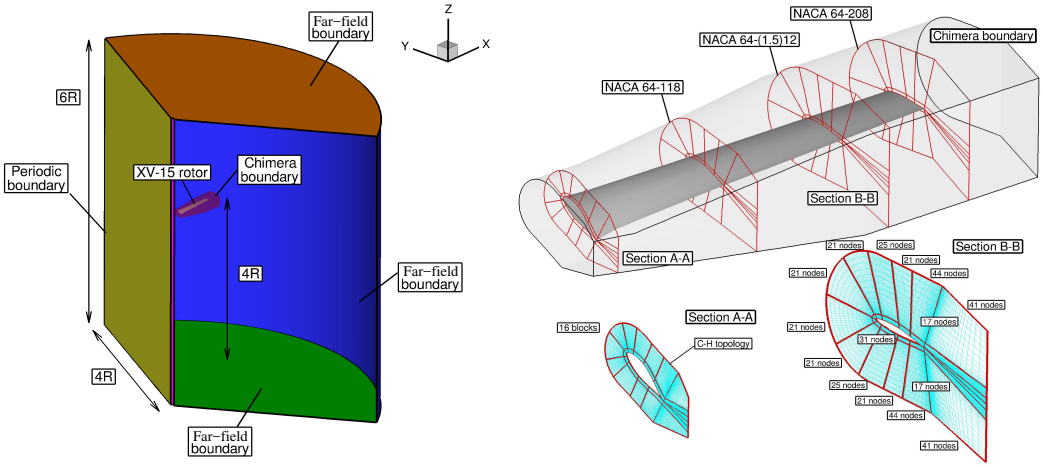

(a) Computational domain. (b) XV-15 rotor mesh.

Figure 3: Computational domain and boundary conditions employed (left) and detailed view of the body-fitted XV-15 rotor mesh (right).

Table 5: Mesh size in million cells for the XV-15 rotor mesh.

	Coarse Mesh	Medium Mesh
Background mesh size	2.6 million	6.0 million
Blade mesh size	3.6 million	3.6 million
Overall mesh size	6.2 million	9.6 million
Wall distance	$1.0 \cdot 10^{-5} c_{\text{ref}}$	$1.0 \cdot 10^{-5} c_{\text{ref}}$

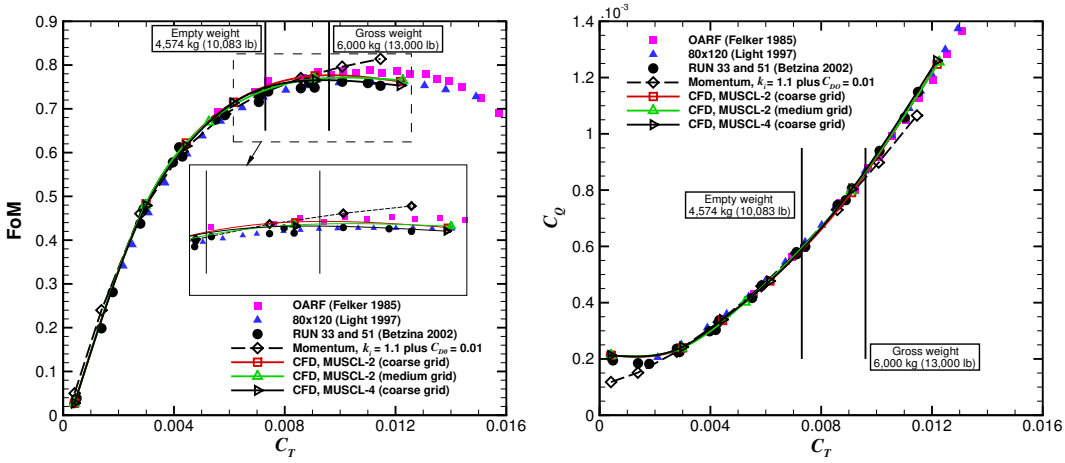

(a) C_T - FoM. (b) C_T - C_Q.

Figure 4: Effect of the MUSCL-2 and MUSCL-4 schemes on the figure of merit (left) and torque coefficient (right) for the full-scale XV-15 rotor.

Table 6: Predicted and experimental [42, 43] figure of merit at blade pitch angle of $10°$.

Case	FoM	Difference [%]
Experiment	0.760	-
MUSCL-2 coarse grid	0.775	1.97%
MUSCL-2 medium grid	0.768	1.05%
MUSCL-4 coarse grid	0.765	0.65%

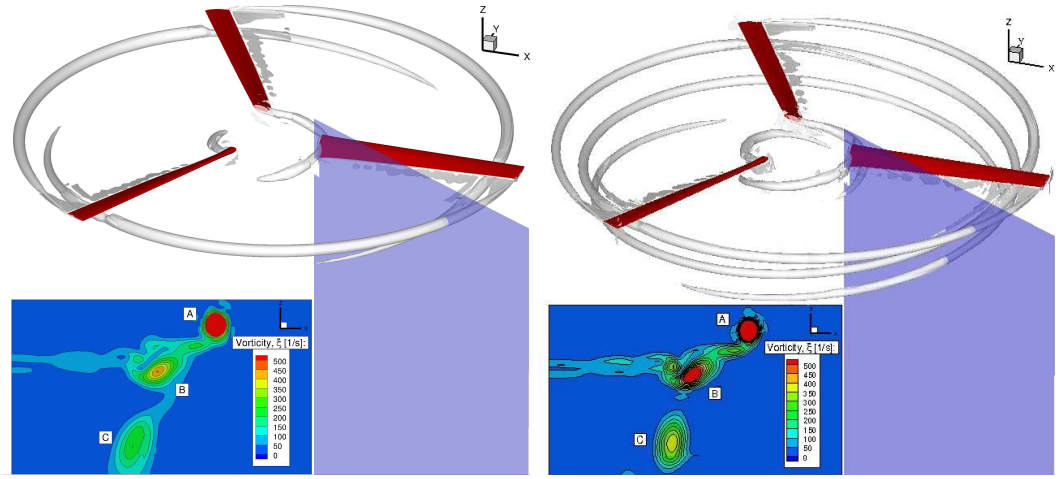

(a) Wake flow using MUSCL-2 scheme. (b) Wake flow using MUSCL-4 scheme.

Figure 5: Wake flowfield for the full-scale XV-15 rotor using $\bar{Q}$-criterion ($\bar{Q}$=0.05). Results with the MUSCL-2 (left) and MUSCL-4 (right) schemes.

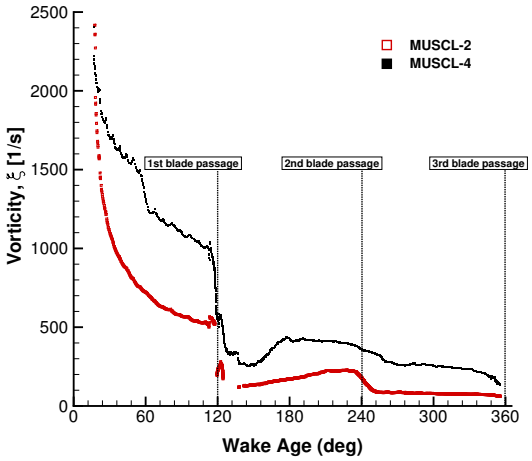

Figure 6: Vorticity of the vortex cores as function of the wake age in degrees obtained with the MUSCL-2 and MUSCL-4 schemes on the coarse grid of Table 5.

Table 7: Geometric properties of the UH-60A rotor [36, 46, 47].

Parameter	Value
Number of blades, N_b	4
Rotor radius, R	321.96 inches
Reference blade chord, c_{ref}	20.76 inches
Aspect ratio, R/c_{ref}	15.5
Rotor solidity, σ	0.0821
Linear twist angle, Θ	-16°

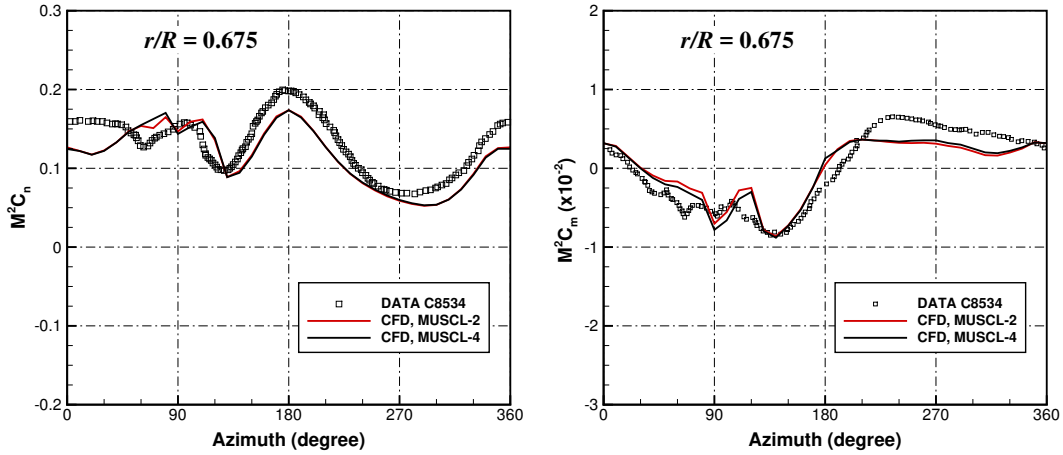

(a) r/R= 0.675.

(b) r/R= 0.675.

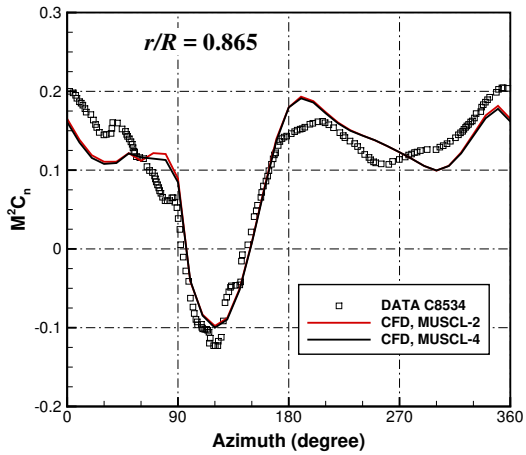

(c) r/R= 0.865.

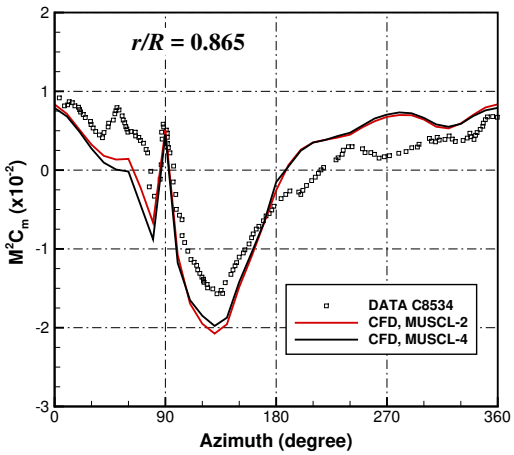

(d) r/R= 0.865.

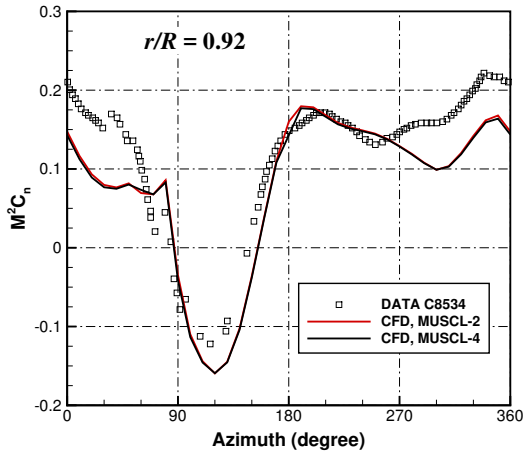

(e) r/R= 0.92.

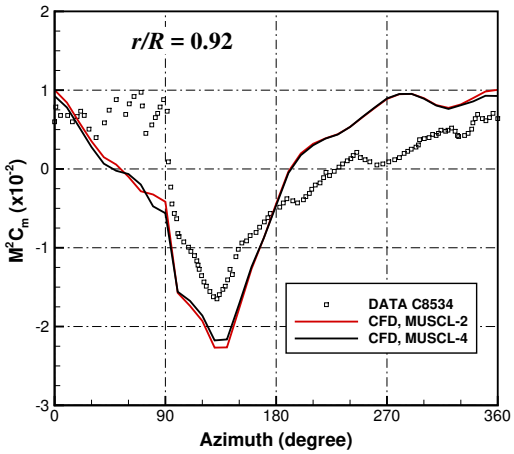

(f) r/R= 0.92.

Figure 7: Comparison between experimental data and predictions using MUSCL-2 and MUSCL-4 schemes for the UH-60A blade normal force and pitch moment (mean removed) at advance ratio (μ= 0.368) at three radial stations.

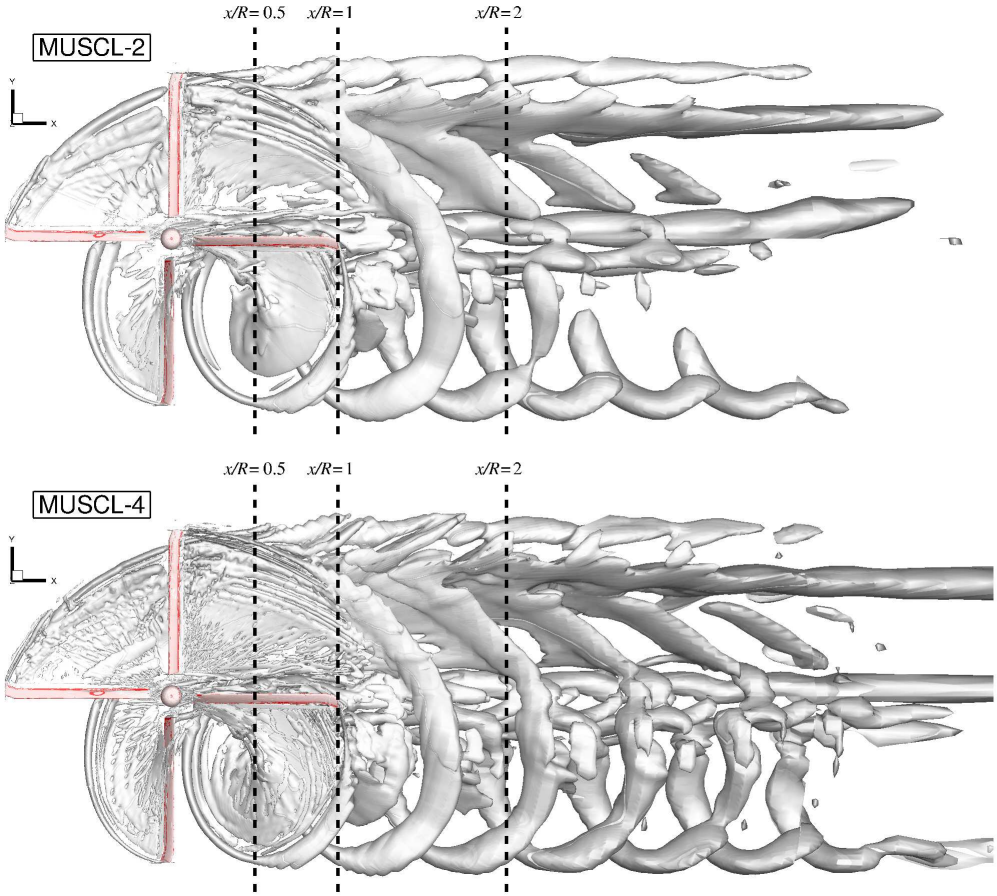

Figure 8: Wake-visualisation of the UH-60A rotor in forward flight using $\bar{Q}$-criterion ($\bar{Q}$=0.0007). Results with the MUSCL-2 (above) and MUSCL-4 (below) schemes.

Table 8: ERICA model-scale component mesh sizes, given as million nodes.

Components	**Million Nodes**
Fuselage and fixed wing	9.9
Nacelle and tiltable wing	30.3
Rotor blades (x4)	11.4
Wind tunnel	4.6
Total	**56.2**

Table 9: Test conditions for the aeroplane mode AC1 [56, 57]. δ_{FU}= fuselage angle of attack; δ_{NAC}= nacelle angle of attack; δ_{TW}= tiltable wing angle of attack.

Parameters	**Value**
M_∞	0.168
M_{tip}	0.470
$\mu = M_\infty / M_{\text{tip}}$	0.357
Re_{ref}	$1.70{\cdot}10^6$
δ_{FU} [deg]	10.02°
δ_{NAC} [deg]	10.02°
δ_{TW} [deg]	10.02°
RPM blade rotor	2130
θ_{75} [deg]	27.36°

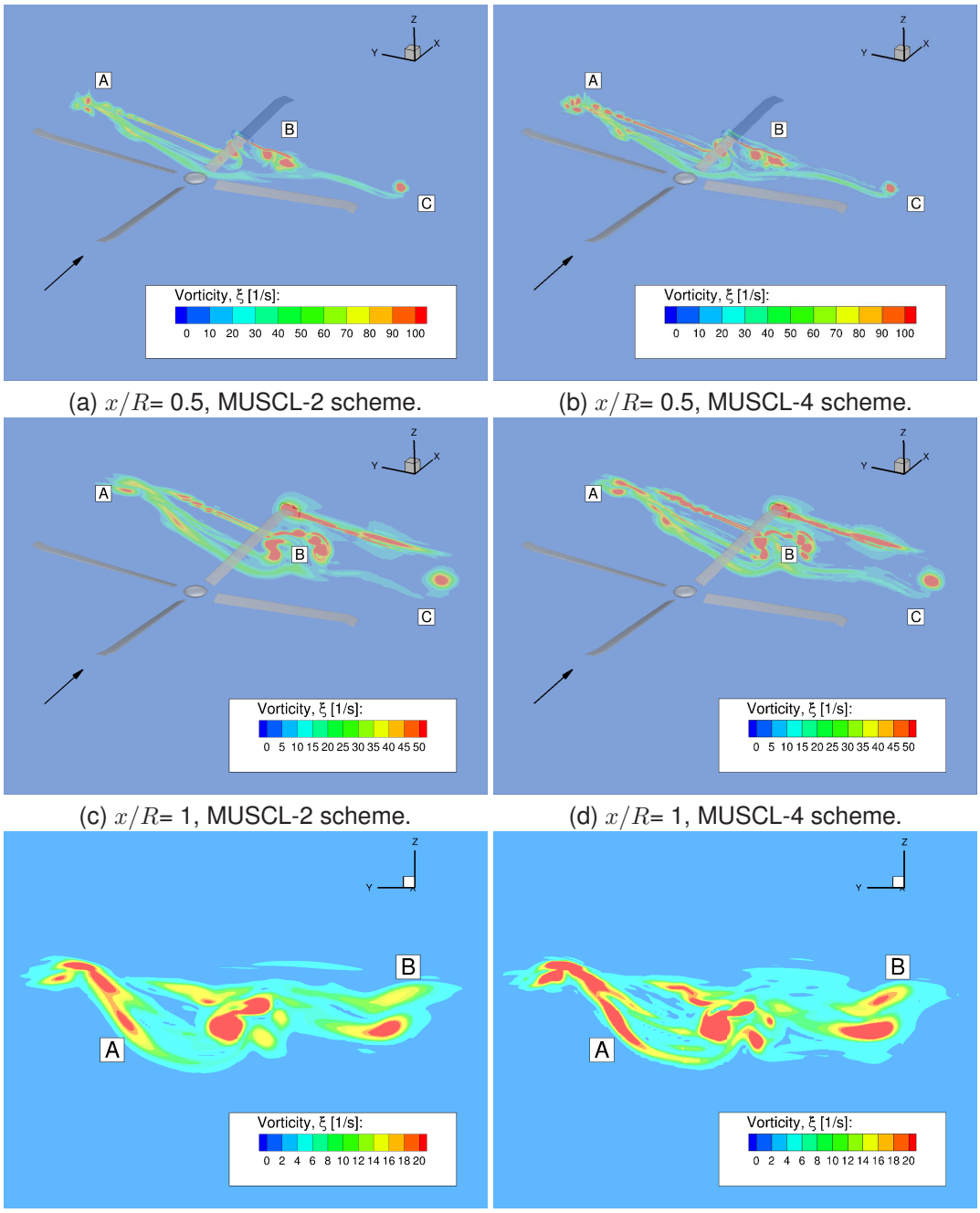

(a) x/R= 0.5, MUSCL-2 scheme.

(b) x/R= 0.5, MUSCL-4 scheme.

(c) x/R= 1, MUSCL-2 scheme.

(d) x/R= 1, MUSCL-4 scheme.

(e) x/R= 2, MUSCL-2 scheme.

(f) x/R= 2, MUSCL-4 scheme.

Figure 9: Vorticity contours at the planes x/R= 0.5, 1, and 2 for the MUSCL-2 and MUSCL-4 schemes.

Table 10: Nomenclature of the stations selected for C_P profile comparisons. FU=Fuselage; FW=Fixed Wing; TW=Tiltable Wing; SYM=Symmetry.

Nomenclature	**Description**
SYM-TOP	Fuselage symmetry plane (top), station y=0 mm.
FW-A	Fixed wing, station y=490 mm.
TW-A	Tiltable wing, station y=855 mm.
TW-B	Tiltable wing, station y=1117.5 mm.

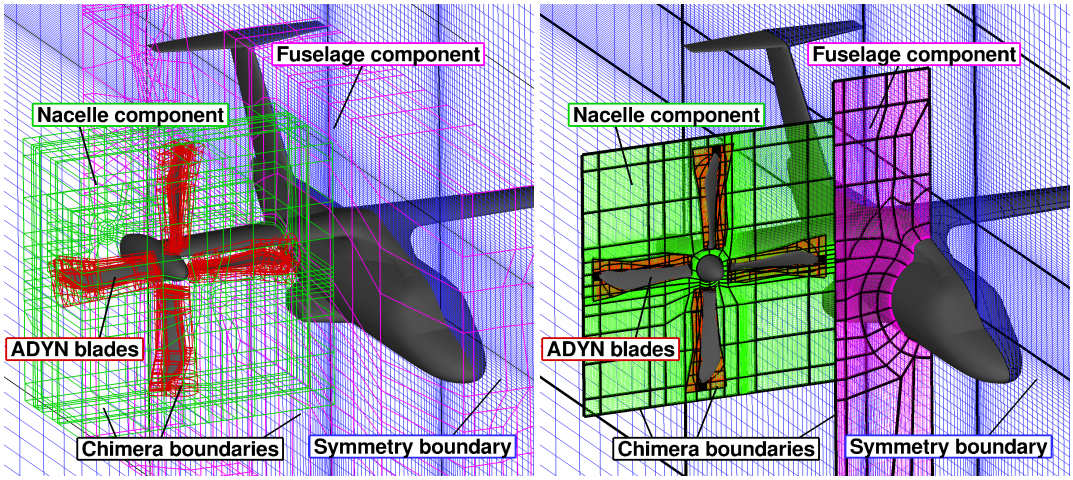

(a) Multi-block grid. (b) Cross section of the multi-block grid.

Figure 10: Details of the multi-block overset arrangement of the ERICA tiltrotor in aeroplane mode configuration. Blue line=background component; Purple line=fuselage component; Green line= nacelle component; Grey line=blade component.

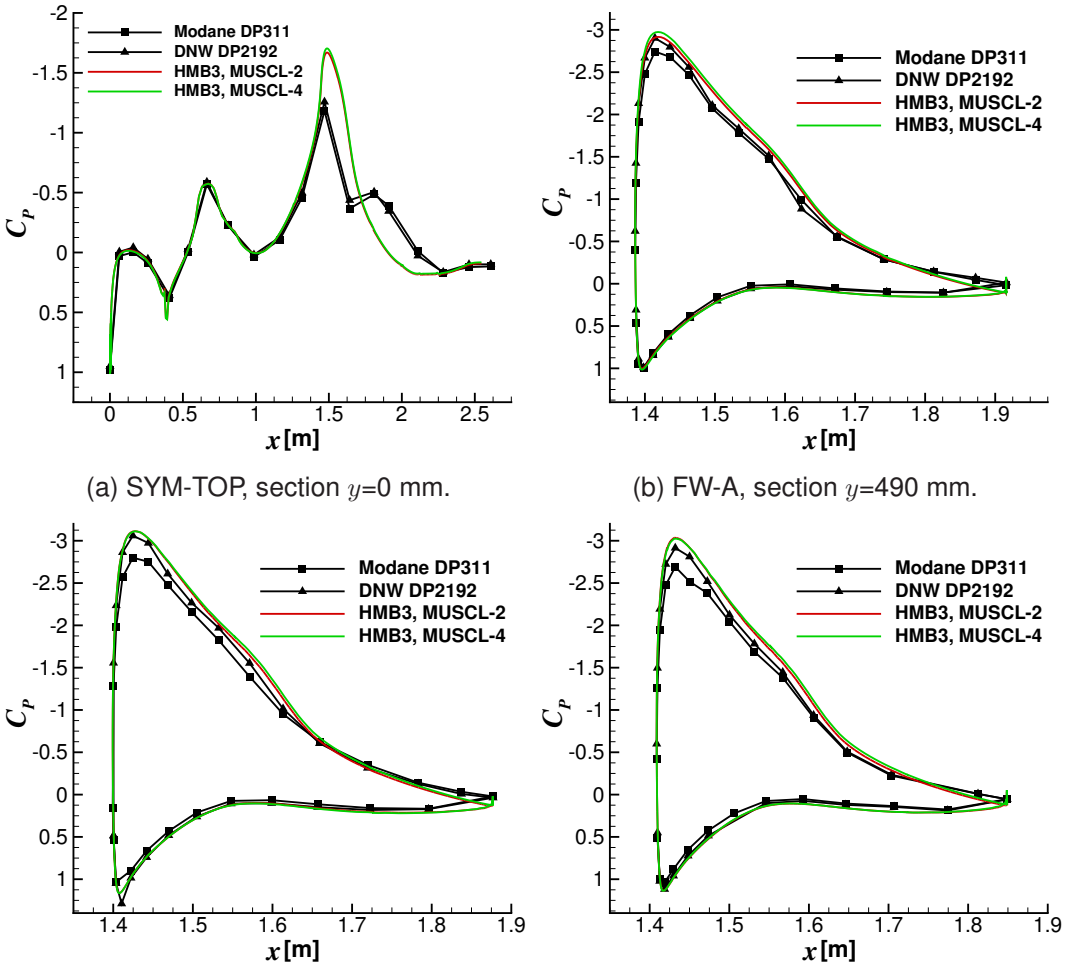

(a) SYM-TOP, section y=0 mm. (b) FW-A, section y=490 mm.

(c) TW-A, section y=855 mm. (d) TW-B, section y=1117.5 mm.

Figure 11: C_P profile comparisons between CFD and experiments [55, 54] on the fixed and tiltable wings of the ERICA tiltrotor for the aeroplane mode configuration AC1.

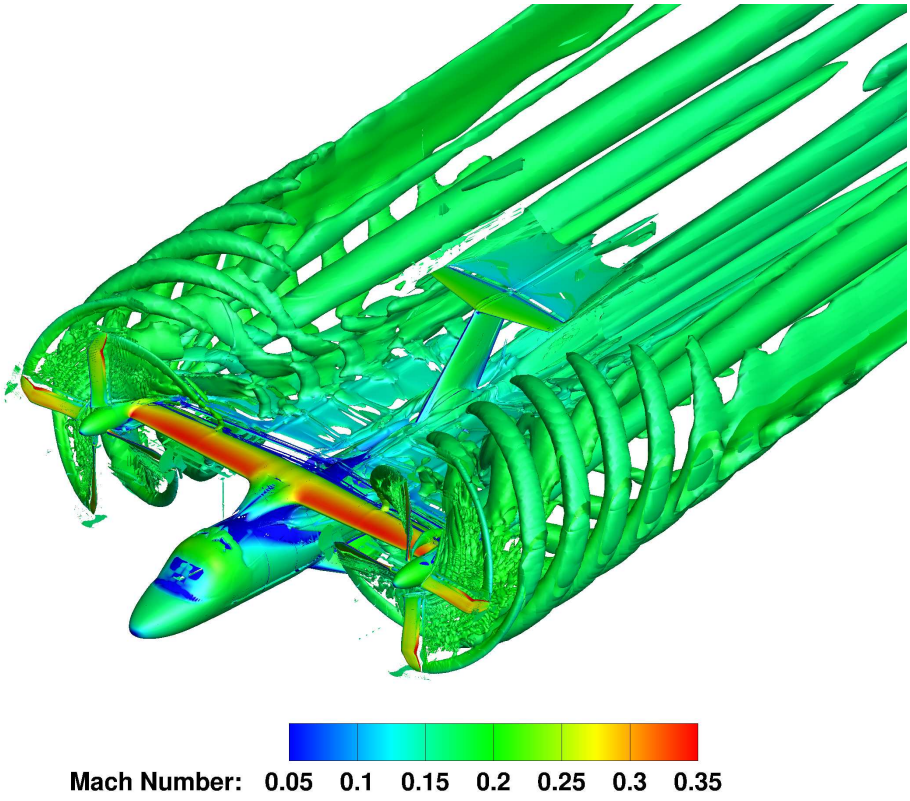

(a) Wake of the MUSCL-2 solution.

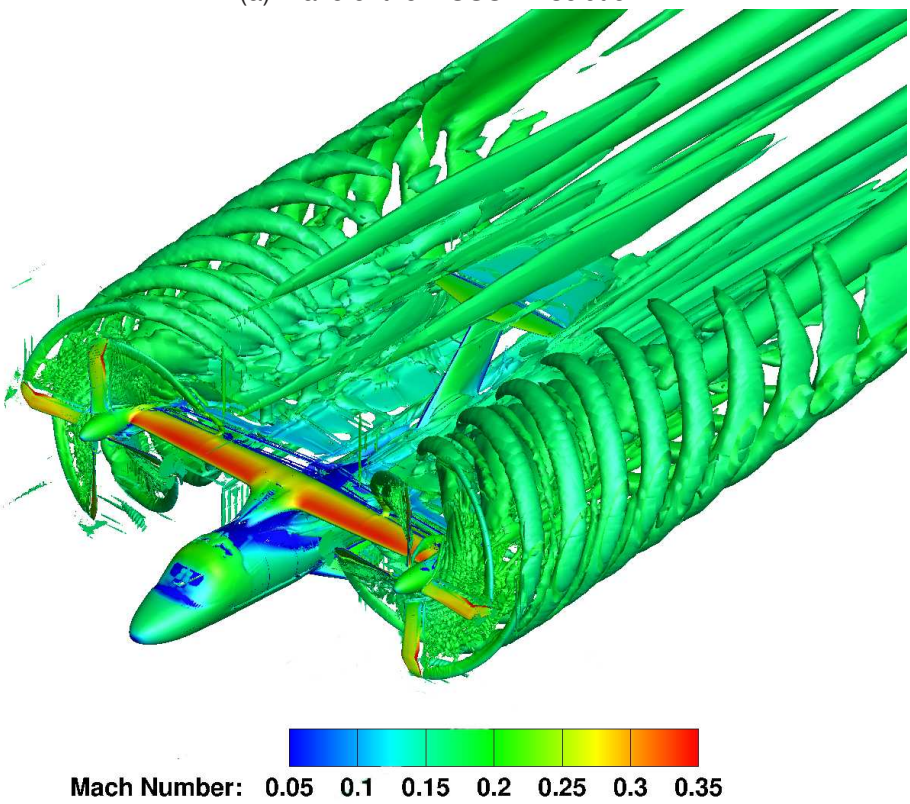

(b) Wake of the MUSCL-4 solution.

Figure 12: Wake-visualisation of the ERICA tiltrotor in aeroplane mode configuration using $\bar{Q}$-criterion ($\bar{Q}$=0.007) shaded by contour of Mach numbers. Results with the MUSCL-2 (above) and MUSCL-4 (below) schemes.